

Improvement of Hyperthermia Properties of Iron Oxide Nanoparticles by Surface Coating

*Original*

Improvement of Hyperthermia Properties of Iron Oxide Nanoparticles by Surface Coating / Vassallo, Marta; Martella, Daniele; Barrera, Gabriele; Celegato, Federica; Coïsson, Marco; Ferrero, Riccardo; Olivetti, Elena S.; Troia, Adriano; Sözeri, Hüseyin; Parmeggiani, Camilla; Wiersma, Diederik S.; Tiberto, Paola; Manzin, Alessandra. - In: ACS OMEGA. - ISSN 2470-1343. - ELETTRONICO. - 8:2(2023), pp. 2143-2154. [10.1021/acsomega.2c06244]

*Availability:*

This version is available at: 11583/2974583 since: 2023-01-13T10:20:17Z

*Publisher:*

American Chemical Society

*Published*

DOI:10.1021/acsomega.2c06244

*Terms of use:*

This article is made available under terms and conditions as specified in the corresponding bibliographic description in the repository

*Publisher copyright*

(Article begins on next page)

# Improvement of hyperthermia properties of iron oxide nanoparticles by surface coating

*Marta Vassallo\**, *Daniele Martella*, *Gabriele Barrera*, *Federica Celegato*, *Marco Coisson*,  
*Riccardo Ferrero*, *Adriano Troia*, *Hüseyin Sözeri*, *Camilla Parmeggiani*, *Diederik S. Wiersma*,  
*Paola Tiberto*, *Alessandra Manzin\**

**ABSTRACT:** Magnetic hyperthermia is an oncological therapy that exploits magnetic nanoparticles activated by radiofrequency magnetic fields to produce a controlled temperature increase in a diseased tissue. The specific loss power of magnetic nanoparticles or capability to release heat can be improved by means of surface treatments, which can reduce agglomeration effects, thus impacting on local magnetostatic interactions. In this work, Fe<sub>3</sub>O<sub>4</sub> nanoparticles are synthesized via co-precipitation reaction and fully characterized in terms of structural, morphological, dimensional, magnetic and hyperthermia properties (under Hergt-Dutz limit). Different types of surface coating are tested, comparing their impact on the heating efficacy and colloidal stability. It results that sodium citrate leads to a doubling of the specific loss power with a substantial improvement in dispersion and stability in solution overtime; a specific loss power around 170 W/g is obtained in this case for a 100 kHz and 48 kA/m magnetic field.

**KEYWORDS:** Iron oxide nanoparticles, cancer therapy, magnetic hyperthermia, surface coating, colloidal stability, magnetometry, thermal characterization, specific loss power.

## 1. INTRODUCTION

Magnetic hyperthermia is a therapy that can be used in cancer treatment, generally as adjuvant for chemotherapy or radiotherapy. This technique is based on the use of magnetic nanoparticles (NPs), which are injected or conveyed through the circulatory system in the tumor region and then activated by an alternating current (AC) magnetic field, with the consequent release of thermal energy through hysteresis losses. The aim is to selectively raise the temperature of the tumor region to 40-45 °C, to induce a sensitization of cancer cells to drug or radiation.<sup>1-4</sup> The side effects are limited as healthy cells are less thermosensitive than cancerous ones, being characterized by hypoxia and lower pH.<sup>5,6</sup>

Magnetic hyperthermia is a very versatile technique, which can also be used for other biomedical applications, such as drug delivery (through the controlled release of molecules encapsulated in thermolabile coatings)<sup>4,7,8</sup> or warming of frozen organs for transplantation.<sup>9</sup> Moreover, magnetic hyperthermia can be combined with photothermal therapy, using light and magnetic fields in a synergic way to treat cancer lesions with higher efficacy.<sup>8,10</sup>

The magnetic nanomaterials mostly studied for hyperthermia are iron oxide NPs, due to their chemical stability, easy surface coating and high biocompatibility in terms of safety and body clearance.<sup>2,8,11</sup> The biocompatibility and biosafety of iron oxide NPs have been assessed by numerous cytotoxicity studies, performed on different cell lines.<sup>12</sup> Some formulations based on iron oxide NPs have also been approved by the Food and Drug Administration (FDA) and the European Medicines Agency (EMA) for therapeutic and diagnostic applications, such as treatment of iron deficiency, magnetic resonance imaging (MRI) and cancer therapy.<sup>4,11,12</sup> In particular, clinical studies of magnetic hyperthermia have been already conducted on prostatic carcinoma and

glioblastoma multiforme using NanoTherm® ferrofluid, consisting of iron oxide NPs covered with aminosilane.<sup>13-15</sup>

The capability of magnetic NPs to release heat is generally expressed through the specific loss power (SLP), which is the power dissipated per unit mass of magnetic material.<sup>16</sup> Material properties, size, shape and state of aggregation are the main parameters that can influence the SLP.<sup>17-23</sup> Regarding material properties, a precise tuning of magnetocrystalline anisotropy and applied magnetic field parameters can lead to an increase in the heating efficiency, as documented for spherical cobalt ferrite NPs.<sup>24,25</sup> Size should be accurately modified to obtain an optimum for the heating efficiency, as demonstrated by cubic iron oxide NPs, which show a maximum SLP around 100 nm.<sup>26</sup> Shape has also a key-role; very high values of SLP have been reported for flower-, disk-, ring- and octahedron-like NPs, which however, require controlled pressures and high temperatures<sup>27-30</sup> or nanolithography techniques<sup>31</sup> for their synthesis that are difficult to be scaled-up at industrial level.

Regarding the state of aggregation, the formation of NP clusters or chains driven by magnetostatic dipole-dipole interactions can be responsible for a significant variation in the SLP,<sup>32,33</sup> e.g., the arrangement in chains typically results in larger SLP values,<sup>26</sup> while clusters usually lead to worse heating performance. One of the best strategies to minimize magnetostatic interactions is to functionalize the surface of the NPs with organic or inorganic coatings, which favor their dispersion via the direct creation of a steric hindrance or by conferring a surface charge that triggers repulsive electrostatic interactions.<sup>34-36</sup> The coatings not only increase the colloidal stability, but can also improve the NP biocompatibility, allowing their suspension in aqueous or organic media, and enable the binding with other functional groups or molecules, useful for addressing specific functions in therapeutics and diagnostics.<sup>5,35</sup>

In this paper, we focus on the chemical synthesis, via co-precipitation method, of Fe<sub>3</sub>O<sub>4</sub> NPs and on the functionalization of their surface with non-toxic coating agents based on sodium citrate or carboxymethyl cellulose (CMC), investigated to improve the heating efficiency and colloidal stability of bare NPs. Sodium citrate was chosen for its high biocompatibility, as documented by its large use in the food and pharmaceutical industry<sup>37,38</sup>. Citrate ions have indeed a strong coordination affinity with iron ones, which favors NP chemisorption; moreover, the carboxylate groups can promote the processes of cellular transport and internalization of NPs.<sup>39-41</sup> CMC, a water-soluble polymer derived from cellulose by hydroxyl groups substitution with carboxymethyl groups, was chosen because it can increase blood circulation time. Moreover, the carboxylic groups, not directly bonded on the NP surface, can be used for further functionalization with other molecules, e.g., for targeting in drug delivery.<sup>42-44</sup>

The prepared NPs were first characterized in terms of structural, morphological, and dimensional properties by means of X-ray Diffractometry (XRD) and Transmission Electron Microscope (TEM) imaging. The effective presence of surface coating was analyzed via Fourier Transform Infrared (FTIR) spectroscopy and Thermogravimetric Analysis (TGA), followed by the investigation of colloidal stability and hydrodynamic size through Dynamic Light Scattering (DLS). Magnetic properties were studied in detail, measuring both the static hysteresis loops of dry samples and the dynamic hysteresis loops of liquid samples. The latter results were correlated with the outputs from thermometric characterization, performed under a 100 kHz magnetic field with amplitude varied up to 48 kA/m. In this way, we guaranteed the satisfaction of the Hergt-Dutz limit, that is  $\hat{H}_a \times f \leq 5 \cdot 10^9 \text{ A}/(\text{m} \cdot \text{s})$ ,<sup>45,46</sup> where  $\hat{H}_a$  and  $f$  are the peak amplitude and frequency of the applied AC magnetic field, respectively. Above this limit, non-negligible eddy current effects associated with heating of healthy tissues were previously observed in pre-clinical tests

conducted on mice and rats<sup>47</sup> as well as predicted by *in silico* models<sup>48</sup>. The SLP values estimated from thermometric characterization were finally corroborated by thermal simulations performed with an in-house heat transfer solver.<sup>49</sup>

## **2. EXPERIMENTAL SECTION**

### **2.1. Materials.**

All materials employed for sample preparation, i.e. iron(II) chloride tetrahydrate ( $\text{FeCl}_2 \cdot 4\text{H}_2\text{O}$ ), iron(III) chloride hexahydrate ( $\text{FeCl}_3 \cdot 6\text{H}_2\text{O}$ ), ammonium hydroxide solution ( $\text{NH}_4\text{OH}$ , 30%), sodium carboxymethyl cellulose (average  $M_w \sim 90$  kDa) and tri-sodium citrate dihydrate ( $\text{C}_6\text{H}_5\text{Na}_3\text{O}_7 \cdot 2\text{H}_2\text{O}$ ), were purchased from Sigma-Aldrich and used without further purification.

### **2.2. Synthesis and Surface Coating.**

$\text{Fe}_3\text{O}_4$  NPs were synthesized through the co-precipitation method.<sup>50</sup> Briefly, iron(II) chloride tetrahydrate and iron(III) chloride hexahydrate were dissolved in deionized water with a molar ratio of  $\text{Fe}^{2+}/\text{Fe}^{3+}$  equal to 1:2 and an iron concentration of 0.5 M. The reaction was carried out in a total volume of 100 mL of water under vigorous stirring and nitrogen flow for its entire duration. Following the complete dissolution, the mixture was heated to 75 °C and precipitation was achieved by adding a 15 mL solution of ammonium hydroxide (30%) dropwise to reach the pH of 8.0-8.5. The precipitate was heated to 85 °C for 1 h, washed with deionized water until neutral pH is reached and magnetically decanted, to separate the synthesized  $\text{Fe}_3\text{O}_4$  NPs.

For the citrate coating, dried  $\text{Fe}_3\text{O}_4$  NPs were suspended in 50 mL of water (2% w/v) and sonicated for 10 min. An aqueous solution 4% w/v of tri-sodium citrate dihydrate was prepared under stirring and added to the above suspension with a molar ratio of 6.4 ( $\text{Fe}_3\text{O}_4/\text{citrate}$ ). The

obtained mixture was sonicated in a sonicator bath and heated to 60 °C for 1 h. The material was washed three times with deionized water and recovered by magnetic separation.

For the CMC coating, dried Fe<sub>3</sub>O<sub>4</sub> NPs were suspended in 15 mL water (1% w/v) and sonicated for 10 min. An aqueous solution 0.1% w/v of CMC (10 mL) was obtained under stirring and added dropwise to the magnetic suspension. The mixture was stirred overnight, and the Fe<sub>3</sub>O<sub>4</sub> NPs were collected magnetically and washed three times with deionized water.

### **2.3. Structural, Morphological and Dimensional Characterization.**

The crystal phase of the Fe<sub>3</sub>O<sub>4</sub> NPs was analyzed by X-ray Diffractometry (XRD), using the Shimadzu - XRD-6000 diffractometer with Cu-K $\alpha$  radiation in the 2 $\theta$  range from 20° to 80°. The obtained XRD spectrum was refined using the Rietveld method and compared with the data provided for Fe<sub>3</sub>O<sub>4</sub> in the JCPDS card No. 19-0629.

Morphology and size distribution of the Fe<sub>3</sub>O<sub>4</sub> NPs were determined by means of Transmission Electron Microscope (TEM), employing the JEOL - JEM-2100 TEM. TEM images were analyzed with the open-source ImageJ software;<sup>51</sup> the mean size was estimated performing statistical analysis on 160 NPs.

### **2.4. Characterization of Surface Coating and Colloidal Stability.**

The presence of a coating bounded to the surface of the Fe<sub>3</sub>O<sub>4</sub> NPs was investigated by Fourier Transform Infrared (FTIR) spectroscopy using the Shimadzu - FT-IR spectrometer, model IRAffinity-1S.

The composition of the Fe<sub>3</sub>O<sub>4</sub> NPs was determined by Thermogravimetric Analysis (TGA) employing the TA Instruments - Discovery SDT 650 analyzer, operating with a temperature ramp up to 1000 °C, applying a constant heating rate of 10 °C/min. TGA results enabled the evaluation of the amount of coating bounded to the surface of the NPs.

The colloidal stability and hydrodynamic size of the Fe<sub>3</sub>O<sub>4</sub> NPs were investigated by Dynamic Light Scattering (DLS) using the Beckman Coulter - Delsa™Nano Zeta Potential and Submicron Particle Size analyzer. DLS results were obtained with at least three scans for each measurement.

The above instrument was also used to evaluate the surface charge of the Fe<sub>3</sub>O<sub>4</sub> NPs by zeta potential measurements conducted on the magnetic suspensions at neutral pH. Zeta potential results were obtained with at least three scans for each measurement.

Colloidal stability was also monitored in time by observing the NP suspensions after 6 months following their preparation and by characterizing the NPs encapsulated in hydrogels. For the encapsulation, agarose was added to an aqueous suspension of Fe<sub>3</sub>O<sub>4</sub> NPs, with a concentration of 5 mg/mL, to obtain a concentration of 1% w/v. The mixture was then heated at 80 °C for 10 min to dissolve the agarose and cool down to form the gel.

## **2.5. Magnetic Characterization.**

The static hysteresis loops of dry samples were measured at room temperature by Vibrating Sample Magnetometry (VSM), employing the Lake Shore - 7410 magnetometer. The characterization was performed under direct current (DC) magnetic fields, varying from -1352 kA/m to 1352 kA/m in steps of 0.8 kA/m.

Dynamic hysteresis loops were measured at room temperature by a custom-built B-H tracer,<sup>52</sup> under the application of a uniform AC magnetic field with a frequency of 69 kHz and an amplitude selectable up to 36 kA/m. The measurements were performed on samples constituted by an aqueous suspension of uncoated or coated Fe<sub>3</sub>O<sub>4</sub> NPs with a concentration of 10 mg/mL and 12 mg/mL, respectively.



## 2.6. Thermometric Characterization.

Thermometric measurements were performed with a custom-built setup.<sup>53</sup> The aqueous suspensions of uncoated or coated Fe<sub>3</sub>O<sub>4</sub> NPs, with a concentration of about 12 mg/mL, were poured in a test tube and then exposed to a uniform AC magnetic field with a frequency of 100 kHz and an amplitude selectable in the range 24-48 kA/m, thus satisfying the Hergt-Dutz limit.<sup>45,46</sup> The heating time was fixed to 1 h for each measurement. A fiber optic thermometer (Osensa Innovation), with the sensing point placed in correspondence of the suspension center, was used to measure the local temperature during the heating and cooling transients. Then, the recorded time evolution of the temperature was analyzed by means of a fitting-function derived from an analytical thermodynamic model,<sup>53</sup> allowing the estimation of the NP Specific Loss Power (SLP).

## 2.7. Heat Transfer Modelling.

The thermometric characterization was supported by thermal simulations carried out with an in-house 3D finite element code, which solves the heat transfer equation under the assumption of negligible convection phenomena.<sup>26,49</sup> This results in:

$$\rho C_p \frac{\partial T}{\partial t} = \nabla \cdot k \nabla T + Q_{\text{ext}} + \frac{\text{SLP} \cdot m_{\text{NPs}}}{V_{\text{water}}}, \quad (1)$$

where  $T$  is the temperature,  $\rho$  is the mass density,  $C_p$  is the heat capacity and  $k$  is the thermal conductivity. SLP is the NP specific loss power estimated from the thermometric characterization,  $m_{\text{NPs}}$  is the mass of magnetic NPs within the particle-fluid suspension, where the NPs are assumed to be uniformly dispersed, and  $V_{\text{water}}$  is the water volume.  $Q_{\text{ext}}$  is the heating power per unit volume due to the AC magnetic field source; this includes parasitic eddy current heating effects and is derived from preliminary thermometric measurements performed on a sample of water with volume  $V_{\text{water}}$ .

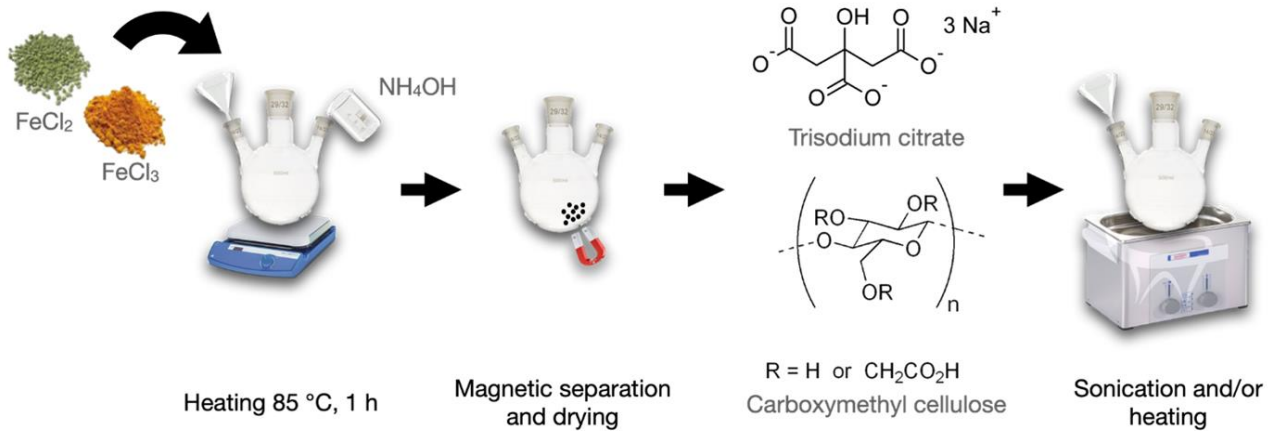


**Figure 1.** Schematic representation of the chemical preparation via co-precipitation and coating with trisodium citrate or CMC of Fe<sub>3</sub>O<sub>4</sub> NPs.

Equation (1) is completed by the following boundary condition:

$$k\nabla T \cdot \mathbf{n} = h(T_{\text{ext}} - T), \quad (2)$$

where  $\mathbf{n}$  is the outward normal vector to the boundary surface,  $h$  is the heat transfer coefficient, which considers convective cooling effects, and  $T_{\text{ext}}$  is the time-dependent external temperature. At  $t = 0$ ,  $T = T_{\text{ext}}$  in all the domain of analysis.

### 3. RESULTS AND DISCUSSION

#### 3.1. Preparation and Surface Coating of Fe<sub>3</sub>O<sub>4</sub> Nanoparticles.

A schematic of the Fe<sub>3</sub>O<sub>4</sub> NP synthesis and coating is reported in Figure 1. The synthesis was performed with a simple and large-scale process that involves co-precipitation in alkaline environment. Starting from a mixture containing Fe<sup>2+</sup> and Fe<sup>3+</sup>, the NPs were precipitated with ammonium hydroxide solution and heated up to 85 °C. After magnetic recovery and washing with water, a large quantity of NPs was obtained, corresponding to a yield of 72.7 % (mass of 1.7 g). The reproducibility of the co-precipitation method was verified by synthesizing a second batch of

Fe<sub>3</sub>O<sub>4</sub> NPs using the same synthesis conditions described above. To test the reproducibility in terms of heating properties, we performed also on this sample magnetic and thermometric characterizations (as described in the following Sub-sections).

Moreover, surface coating processes were performed with the aim of modifying the colloidal stability of the NPs and thus improving their hyperthermia properties. A solution of the coating agent (tri-sodium citrate or CMC) was added to a Fe<sub>3</sub>O<sub>4</sub> NP suspension and subjected to heating and/or sonication. The NPs were purified another time by magnetic decantation and washing with water.

### **3.2. Analysis of Crystal Phase, Dimension, Surface Coating and Colloidal Stability.**

Dried Fe<sub>3</sub>O<sub>4</sub> NPs were first characterized in terms of crystal structure, size, and shape. The XRD spectrum for uncoated NPs is shown in Figure 2A, revealing a crystalline phase with the diffraction peaks indexed as (220), (311), (400), (422), (511) and (440), like for the cubic spinel structure of Fe<sub>3</sub>O<sub>4</sub> (JCPDS card No. 19-0629).

Representative TEM images of uncoated and citrate-coated Fe<sub>3</sub>O<sub>4</sub> NPs are reported in Figures 2B and 2C, respectively (the corresponding image for CMC-coated Fe<sub>3</sub>O<sub>4</sub> NPs is shown in Figure S1). The NPs have a quasi-spherical shape and are strongly uniform in size, exhibiting a narrow size distribution well fitted by a log-normal distribution function with a mean value of 10.9 nm and a standard deviation of 2.6 nm. This is well demonstrated by the histogram in Figure 2D, derived from statistical analysis of TEM images performed on the Fe<sub>3</sub>O<sub>4</sub> NPs by means of ImageJ software.<sup>51</sup> From TEM images, it is also possible to observe differences in the aggregation state of the samples. The uncoated Fe<sub>3</sub>O<sub>4</sub> NPs are arranged in aggregates with dimensions around 130 nm (Figure 2B), as a possible consequence of strong magnetic dipole-dipole interactions. Similar

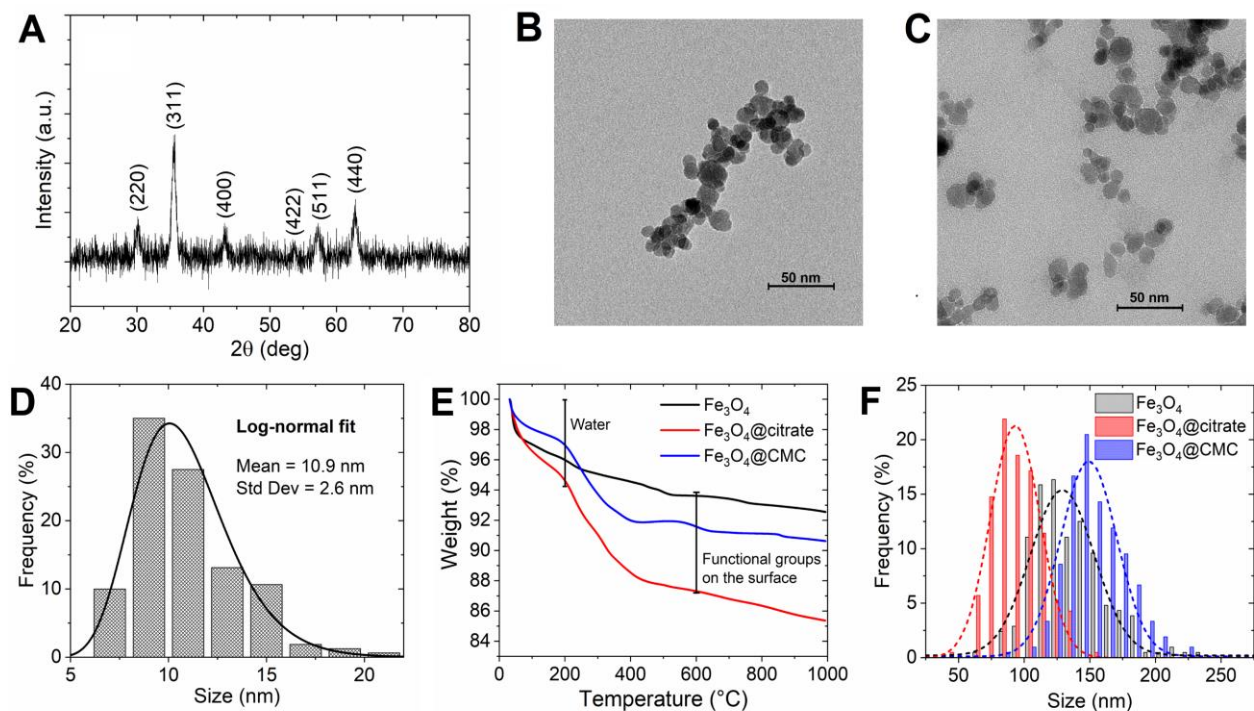


**Figure 2.** (A) XRD spectrum of the uncoated  $\text{Fe}_3\text{O}_4$  NPs. Representative TEM images of (B) uncoated and (C) citrate-coated NPs; (D) size distribution histogram (derived from statistics analysis on TEM images of uncoated NPs). (E) TGA curves and (F) DLS particle size distribution for uncoated (black), citrate-coated (red) and CMC-coated (blue) NPs (the reported Gaussian fits are a guide to the eye).

aggregates are observed for the CMC-coated  $\text{Fe}_3\text{O}_4$  NPs (Figure S1), while those with the citrate-based coating are clustered in smaller aggregates (Figure 2C).

The presence of surface coating, based on tri-sodium citrate or CMC, was confirmed by different characterization techniques, comprising FTIR spectroscopy, TGA and DLS analysis. The FTIR spectra of uncoated and coated  $\text{Fe}_3\text{O}_4$  NPs are shown in the Supporting Information in Figure S2. For the uncoated NPs, the measured spectra are typical of  $\text{Fe}_3\text{O}_4$  NPs, where the band at  $580\text{-}630\text{ cm}^{-1}$  corresponds to the vibration of the Fe-O bond, while the peaks at  $1624\text{ cm}^{-1}$  and  $3400\text{ cm}^{-1}$  can be attributed to the bending and stretching vibrations of the hydroxyl groups of the water molecules adsorbed on the sample surface.<sup>43</sup> In the spectra of the citrate- and CMC-coated NPs, two and three new peaks appear, at  $(1381, 1616)\text{ cm}^{-1}$  and  $(1059, 1417, 1623)\text{ cm}^{-1}$ , respectively.

The peaks at  $1381\text{ cm}^{-1}$  and  $1616\text{ cm}^{-1}$  can be attributed to symmetric and asymmetric stretching vibration of  $\text{COO}^-$  groups of citrate anions, respectively.<sup>54,55</sup> The peaks at  $1059\text{ cm}^{-1}$ ,  $1417\text{ cm}^{-1}$  and  $1623\text{ cm}^{-1}$  correspond, in the order, to stretching vibration of O-C-C bond, and to symmetric and asymmetric stretching vibration of -COO bond in the structure of carboxylic salt. The new peak presence demonstrates that the coating agents were effectively bonded to the surface of the  $\text{Fe}_3\text{O}_4$  NPs.<sup>43,44,56</sup>

The thermographs of uncoated and coated  $\text{Fe}_3\text{O}_4$  NPs, obtained with TGA, are shown in Figure 2E. The initial weight loss at temperatures below  $200\text{ }^\circ\text{C}$  refers to the desorption of water molecules. The thermogravimetric curve of the uncoated NPs shows that the weight loss in this range is about 4%, while those of the coated NPs report a weight loss of 5.4% and 3% for citrate- and CMC-coated  $\text{Fe}_3\text{O}_4$  NPs, respectively; these small variations are simply due to a different content of water molecules in the samples. The following weight loss for temperatures between  $200\text{ }^\circ\text{C}$  and  $1000\text{ }^\circ\text{C}$  is due to the decomposition of the coating agent adsorbed on the surface of the NPs. This is in the order of 9.2% and 6.4% for citrate- and CMC-coated NPs, respectively; the observed weight loss indicates that a greater quantity of coating agent is adsorbed on the surface of the NPs treated with citrate rather than with CMC.

Finally, we analyzed the stability of NPs in solution, an important parameter for their potential biomedical application. The hydrodynamic size distributions characterized by DLS are shown in

**Table 1.** Mean hydrodynamic size (derived from Gaussian fit), polydispersity index (PDI) and zeta potential values obtained for the three samples (uncoated, citrate- and CMC-coated NPs).

Sample	Mean hydrodynamic size (nm)	PDI	Zeta potential (mV)
Fe <sub>3</sub> O <sub>4</sub>	135.2 ± 34.6	0.277	-24.8 ± 0.5
Fe <sub>3</sub> O <sub>4</sub> @citrate	95.5 ± 18.2	0.251	-26.1 ± 1.4
Fe <sub>3</sub> O <sub>4</sub> @CMC	151.6 ± 26.9	0.276	-26.8 ± 1.0

Figure 2F, and the mean hydrodynamic size, the relative polydispersity index and the zeta potential value of each sample are reported in Table 1. DLS and zeta potential measurements were performed on both uncoated and coated NPs to investigate possible changes in sample dispersion resulting from the surface coating process. Via DLS it is possible to characterize the hydrodynamic behavior of NPs or more precisely the size of the aggregates in which they are organized; however, this technique does not allow us to discriminate between the inorganic material and the organic material of the coating. The mean hydrodynamic size for the uncoated NPs was around 135 nm, confirming the size of the aggregates observed in TEM images (Figure 2B). The improvement in the dispersion of the citrate-coated Fe<sub>3</sub>O<sub>4</sub> NPs, caused by a decrease in the aggregate size already documented by the TEM image in Figure 2C, was also demonstrated by the smaller value of the mean hydrodynamic size, which was in the order of 95 nm. Conversely, the CMC-coated NPs are organized in aggregates with larger dimensions than the ones of uncoated NPs, with size in the order of 150 nm. Thus, the introduction of surface coating leads to a variation in the aggregate size, which strongly depends on the coating type, as already demonstrated in the literature via DLS measurements.<sup>57</sup>

The polydispersity index values were comparable between the samples, and this demonstrated that the width of the size distribution was similar, although the hydrodynamic size of the NP aggregates changes because of the surface treatment.

The zeta potential measurements provide an indication of the surface charge of NPs and it is known that for absolute values greater than 30 mV the suspension is characterized by a good colloidal stability and a low tendency to flocculate.<sup>58</sup> The zeta potential for the uncoated NPs, measured at neutral pH, was  $-24.79 \pm 0.48$  mV, in agreement with the values registered for Fe<sub>3</sub>O<sub>4</sub> NPs.<sup>59</sup> Zeta potentials of  $-26.09 \pm 1.38$  mV and  $-26.79 \pm 1.03$  mV were obtained for the citrate- and CMC-coated NPs.

The above increase in the absolute value of the zeta potential, although modest, demonstrated the adsorption of negatively charged carboxylic groups on the NP surface.<sup>42,54</sup> The slight increase in zeta potential should be attributed to the small amount of coating agents on the surface of Fe<sub>3</sub>O<sub>4</sub> NPs, as can also be seen from the TGA results.

### **3.3. Analysis of Static and Dynamic Magnetic Properties.**

The room-temperature  $M(H)$  curves of uncoated, citrate- and CMC-coated Fe<sub>3</sub>O<sub>4</sub> NPs are shown in Figure 3. The measured magnetic signal was normalized to the Fe<sub>3</sub>O<sub>4</sub> mass contained in each sample, after having appropriately subtracted that of the coating using the results from TGA (see

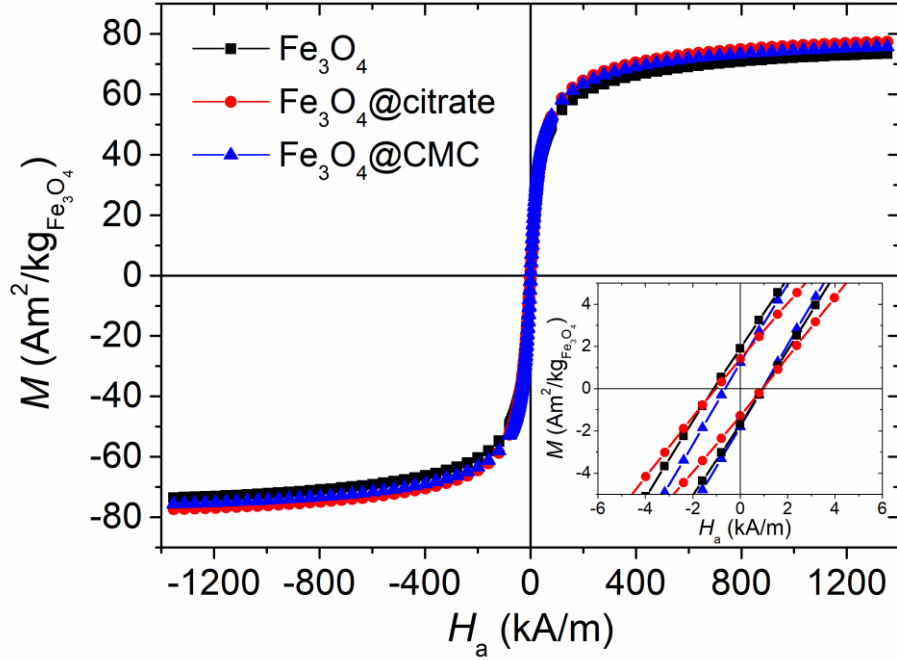


**Figure 3.** Room-temperature  $M(H)$  curves of uncoated and coated  $\text{Fe}_3\text{O}_4$  NPs in dry form. The magnetization values are normalized to the  $\text{Fe}_3\text{O}_4$  mass. A hysteretic behavior can be inferred from the inset, which shows the portion of the hysteresis loops zoomed around coercivity.

Figure 2E). The major hysteresis loops of the three samples practically overlap, as a consequence that the different coatings don't affect the magnetic behavior of the samples in dry form under static conditions. The hysteresis loop of the additionally prepared uncoated  $\text{Fe}_3\text{O}_4$  NPs is reported in Figure S3A, showing practically no differences with respect to the results in Figure 3, as a proof of the reproducibility of the preparation method.

The saturation magnetization ( $M_S$ ) was determined by fitting the large field portion of the hysteresis loops with the well-known expression<sup>60</sup>

$$M = M_S \left( 1 - \frac{\delta}{H_a} - \frac{\lambda}{H_a^2} \right) + \chi H_a, \quad (3)$$



where parameters  $\delta$  and  $\lambda$  were set as free, while  $\chi$  was fixed to zero, since for the considered samples its effect was estimated to be negligible, due to the absence of paramagnetic features.

From Equation (3),  $M_S$  results to be around  $76 \text{ Am}^2/\text{kg}$ ; its lower value, compared to that of bulk magnetite ( $92 \text{ Am}^2/\text{kg}$ ),<sup>61</sup> can be ascribed to effects of canting or disorder of the magnetic spins at the surface of the  $\text{Fe}_3\text{O}_4$  NPs.<sup>62,63</sup> For all samples, the magnetization reversal follows a sigmoidal trend with a very slow approach to saturation, which is not fully reached even at the maximum applied field. In addition, a hysteretic behavior is observed at low applied magnetic fields, resulting in small coercivity  $H_c$  of about  $1 \text{ kA/m}$  (inset of Figure 3). Such features suggest that the samples mainly consist of interacting superparamagnetic NPs.

The above hypothesis is corroborated by TEM and DLS results (Sub-section 3.2.). On one side, the TEM size distribution (see Figure 2D) indicates that the NPs are characterized by an average diameter ( $\sim 10 \text{ nm}$ ) mainly below the critical value ( $d_c$ ) at which the transition from superparamagnetism to ferromagnetism is expected to occur. In particular,  $d_c$  is estimated in the range  $17\text{-}21 \text{ nm}$ , when considering the common values of effective anisotropy for  $\text{Fe}_3\text{O}_4$  ( $2\text{-}4 \cdot 10^4 \text{ J/m}^3$ ).<sup>64-66</sup> Only a small tail of the size distribution exceeds the evaluated  $d_c$  values. Consequently, for practically all the single NPs a superparamagnetic regime should be expected, in which the  $M(H)$  curve follows the non-hysteretic Langevin function (i.e., zero coercivity and remanence). On the other hand, the NP arrangement in aggregates, as revealed by the TEM images (Figures 2B and 2C) and DLS size distribution (Figure 2F), leads to the formation of magnetic structures (with an effective diameter larger than  $d_c$ ), in which the magnetic moments respond coherently to the applied magnetic field, thus inducing the small hysteresis observed under static conditions.<sup>67</sup>

AC magnetometry was then performed to investigate the capability of the NPs to release heat when exposed to AC magnetic fields with frequency  $f$  and peak amplitude  $\hat{H}_a$  satisfying the Hergt-

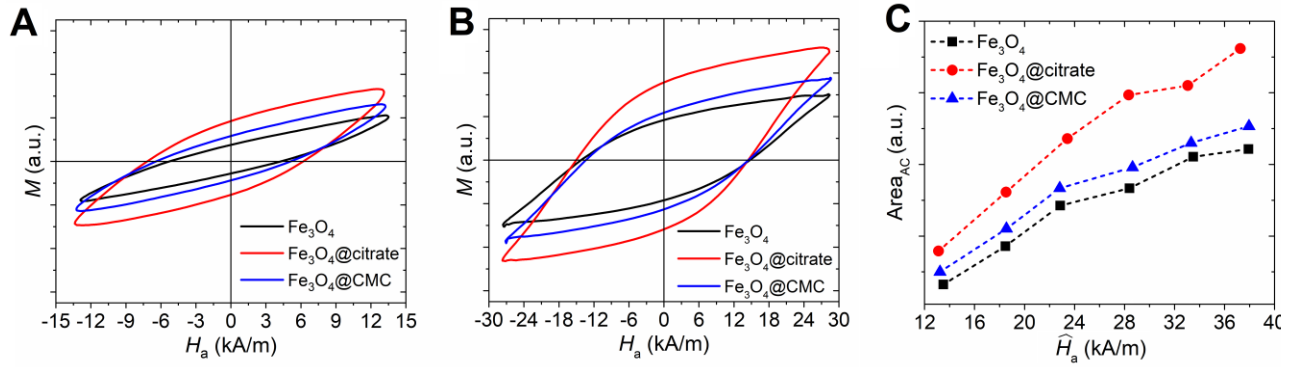


**Figure 4.** Dynamic minor hysteresis loops for uncoated (black), citrate-coated (red) and CMC-coated (blue)  $Fe_3O_4$  NPs, for a magnetic field with peak amplitude  $\hat{H}_a$  of (A) 13.3 kA/m and (B) 28.4 kA/m. All the hysteresis curves are normalized to the sample mass and reported in arbitrary units with the same inferior and superior limits, to enable direct comparison. (C) Areas of the dynamic hysteresis loops versus  $\hat{H}_a$ , evaluated for all the considered samples. All measurements were performed with a frequency of 69 kHz.

Dutz limit.<sup>45,46</sup> In particular, the dynamic hysteresis loops of aqueous suspensions containing both uncoated and coated  $Fe_3O_4$  NPs were measured by applying an AC magnetic field with  $f = 69$  kHz and  $\hat{H}_a$  limited to 36 kA/m. The hysteresis curves for  $\hat{H}_a$  equal to 13.3 kA/m and 28.4 kA/m are reported in Figures 4A and 4B, respectively, while the entire set of AC magnetometry results is provided in Figure S4. The vertical axis is reported in arbitrary units, since the output signal from the custom-built B-H tracer is not related to the magnetization value by a proper calibration procedure. However, all hysteresis curves are normalized to the sample mass to enable the comparison of the magnetic properties of the studied samples.

For all the analyzed cases, the two branches of the hysteresis loops overlap only when the applied magnetic field reaches  $\hat{H}_a$ , thus leading to minor loops. Consequently, the coercivity  $H_c$  of such loops is a function of  $\hat{H}_a$ . However, the values of  $H_c$  result higher than the ones of the corresponding static major hysteresis loops (inset of Figure 3), due to the relaxation effects associated with the

dynamic response to the AC excitation. These effects are responsible for the appearance of a well-defined hysteretic behavior, characterized by loops with a non-negligible area and thus leading to an effective release of energy, which can be exploited for magnetic hyperthermia.<sup>68</sup>

The areas of the dynamic hysteresis loops as a function of  $\hat{H}_a$  are shown in Figure 4C for all the studied samples. The sample containing the citrate-coated Fe<sub>3</sub>O<sub>4</sub> NPs (red curve) is characterized by a larger loop area (i.e., higher heating efficiency) than the other two samples, over the entire range of values considered for  $\hat{H}_a$ . Conversely, the CMC-based coating (blue curve) leads to a small increase in the loop area values, in comparison with the uncoated NPs (black curve). These results may be related to the ability of the citrate-based coating to reduce the size of the NP aggregates, thus improving dispersion properties, as shown in Figure 2F.

### 3.4. Quantitative Analysis of Heating Efficiency.

In addition to AC magnetometry, thermometric measurements were performed to obtain a quantitative estimation of the coating effect on the heating efficiency of the studied NPs. The characterization was performed on liquid suspensions within a polypropylene test tube immersed in a water bath contained in a quartz holder (see the schematic in Figure 5A). As an example, Figures 5B and 5C illustrate the heating-cooling transients for aqueous solutions with the uncoated and citrate-coated Fe<sub>3</sub>O<sub>4</sub> NPs, respectively. The thermal curves were obtained after exposing the NPs for 60 min to an AC magnetic field with a peak amplitude of 48 kA/m and a frequency of 100 kHz, thus satisfying the Hergt-Dutz limit again.<sup>45,46</sup> The concentration of NPs used was of 12 mg/mL to ensure the maintenance of a good stability of the magnetic solution and of temperature values in a suitable range during the measurements.

An analytical thermodynamic model,<sup>53</sup> considering the multiple heat-exchange mechanisms occurring in the experimental setup, was used to fit the experimental curves and estimate the NP

specific loss power (SLP), as a measure of their heating efficiency. The obtained results were corroborated by the simulations carried out with the heat-transfer finite element solver described in Sub-section 2.7, allowing us to determine the spatial distribution of the temperature within the magnetic suspension during the heating-cooling transients. The numerical simulations were performed under non-adiabatic conditions on the system schematized in Figure 5A, considering the following material properties:

- polypropylene test tube:  $\rho = 2600 \text{ kg/m}^3$ ;  $C_p = 820 \text{ J/(kg K)}$ ;  $k = 3 \text{ W/(m K)}$ ;
- quartz holder:  $\rho = 905 \text{ kg/m}^3$ ;  $C_p = 1900 \text{ J/(kg K)}$ ;  $k = 0.185 \text{ W/(m K)}$ ;
- magnetic suspension:  $\rho = 1020 \text{ kg/m}^3$ ;  $C_p = 4086 \text{ J/(kg K)}$ ;  $k = 0.61 \text{ W/(m K)}$ .

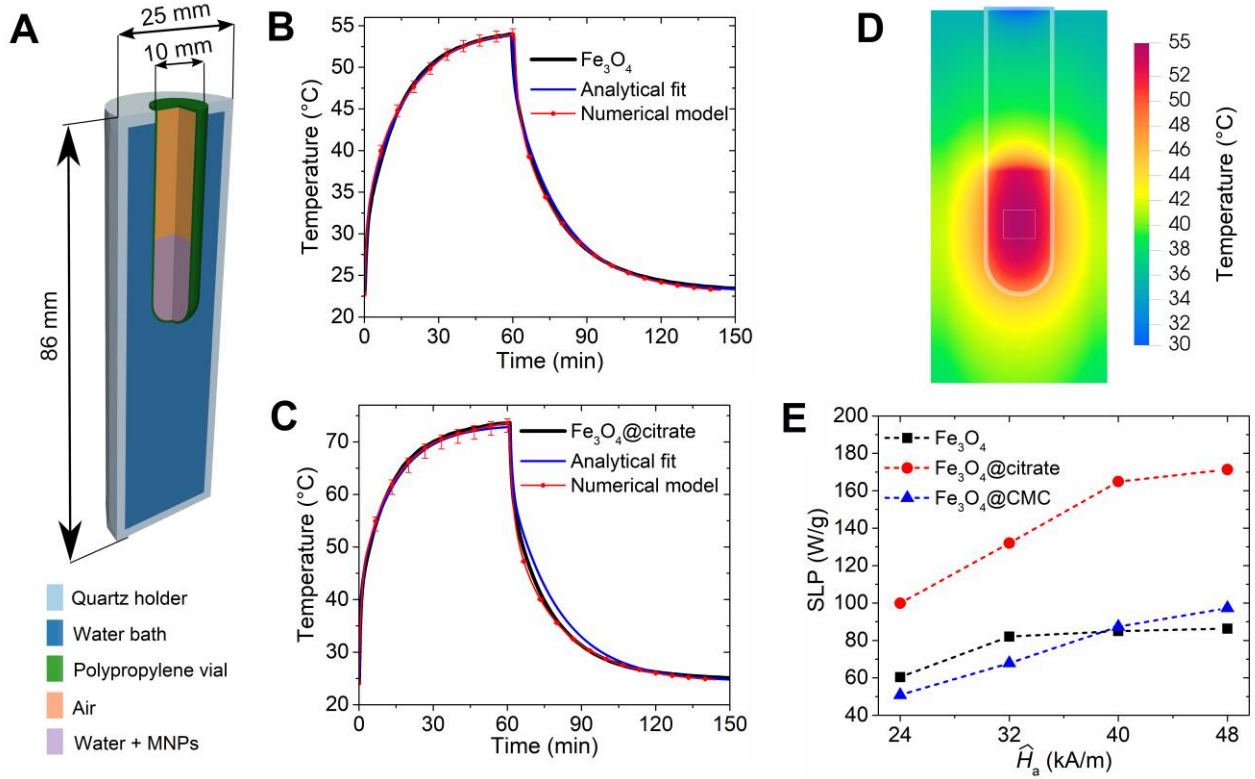


**Figure 5.** (A) Schematic of the sample container, corresponding to the domain considered for heat transfer numerical modelling. Time evolutions of the temperature of the magnetic suspensions containing (B) the uncoated NPs and (C) the citrate-coated NPs, following the application for 60 min of an AC magnetic field with a peak amplitude of 48 kA/m and a frequency of 100 kHz. The graphs contain the experimental data, the best fit outputs of the analytical thermodynamic model and the results obtained with the heat-transfer numerical model. (D) Spatial distribution of the temperature, calculated for the uncoated NP sample at the end of the heating interval. (E) SLP values for uncoated and coated NPs obtained at different peak amplitudes of the AC magnetic field, fixing the frequency to 100 kHz.

The coefficient of convective exchange  $h$  between the holder surface and the surrounding air was set at 14 W/( $\text{m}^2$  K). The heating power  $Q_{\text{ext}}$  produced by the AC magnetic field sources was estimated to be 45 kW/ $\text{m}^3$ , from preliminary thermometric measurements on the only water.

The fitting analytical curves and the numerical results are reported in Figures 5B and 5C, demonstrating a good reconstruction of the experimental data for both the uncoated and citrate-coated NP suspensions. In particular, the numerical curves were calculated in correspondence of the magnetic suspension center, where the sensing point of the fiber optic thermometer is expected

to be placed. The uncertainty bars refer to the temperature variations within a volume around the suspension center, as depicted in Figure 5D, which illustrates the temperature map at the end of the heating phase for the sample containing the uncoated NPs.

The SLP values, derived from the experimental data fitting and validated via numerical modelling, are reported in Figure 5E and Table S1 as a function of  $\hat{H}_a$  for all the considered samples. The SLP values of the additionally prepared uncoated Fe<sub>3</sub>O<sub>4</sub> NPs are reported in Figure S3B, showing negligible differences with respect to the results in Figure 5E, as an ulterior proof of the reproducibility of the preparation method.

In accordance with the outcomes of dynamic hysteresis loop measurements (see Figure 4), the citrate-coated NPs are the most thermally efficient ones in all the considered range of  $\hat{H}_a$ , showing an SLP close to 170 W/g when  $\hat{H}_a = 48$  kA/m (50% larger than the one of uncoated NPs). Conversely, the CMC-coated NPs don't lead to a substantial improvement in the heating efficiency. When  $\hat{H}_a = 48$  kA/m, they approach 100 W/g with an increasing trend, while the uncoated NPs show an SLP in the order of 85 W/g, already reached at 32 kA/m.

These results on the heating efficiency are mainly related to the Néel relaxation mechanism, although the thermometric measurements were performed on NPs dispersed in liquid, the Brown relaxation mechanism is indeed hindered by the large hydrodynamic volume of the NP aggregates (Figure 2F). In particular, the Brown relaxation time roughly estimated for each sample is orders of magnitude longer than the relaxation time  $\tau = 1/(2\pi f)$  related to the used operating frequency, thus resulting in a negligible effect.<sup>69</sup> The heating contribution from the Néel relaxation mechanism is influenced by the effective volume of the magnetic structures that coherently respond to the AC magnetic field. The variations in the SLP values between the citrate-coated NPs and the other two samples can be attributed to the different size of the NP aggregates (95 nm

against 130 nm and 150 nm for the uncoated and CMC-coated NPs). In fact, a simple model proved that the heating efficiency in samples containing clusters of NPs with a diameter lower than 15 nm decreases as the size of the aggregate increases (i.e., if the number of NPs in the aggregate increases).<sup>70</sup>

**Table 2.** Comparison of the results from our study to data from the literature regarding the heating efficiency of spherical Fe<sub>3</sub>O<sub>4</sub> NPs.

Reference	Size (nm)	Coating	Coating procedure	$\dot{H}_a$ (kA/m)	$f$ (kHz)	SLP (W/g)
Our study	10	/	/	48	100	86.3
		Citrate	Post			171
		CMC				97
[71]	13	/	/	15.9	252	63.4
		Citric acid	Post			65.8
		APTES				67.2
		Dextran				55.6
[72]	8.5	/	/	24	418	125
		Oleic acid	Post			60
		Citrate				120
[73]	21.8	/	/		265	80
	15.1	Chitosan	Post			118.85
[74]	20	/	/	26.6	265	38.4
	5	Oleic acid	Post			33.5
	10	PEG				28.3
[75]	21	/	/	23.9	765	440
	8	Citrate	<i>In situ</i>			190
	20	CTAB				95
	22	Dextran				360
[76]	12.5	/	/	13.5	333	100
	5.9	Dextran	<i>In situ</i>			36
	11	Polyvinyl pyrrolidone (PVP)				160
	9.5	PEG				70
	5	Polyacrylic acid (PAA)				2
	7.5	Hyaluronic acid (HA)				40
[77]	8	/	/	23.5	312	39.5
	9.3	Oleic acid 0.2%	<i>In situ</i>			34.81
	8.3	Oleic acid 0.5%		23.36		
	10	Oleic acid 1.0%		45.98		
[78]	10.2	/	/	14.7	276	30
	11.7	Fucoidan	Post			156
	6.4	Fucoidan	<i>In situ</i>			100



In summary, the 50% increase in SLP achieved with the citrate-based surface treatment after preparation is a very promising result, also in comparison with the data available in the literature for spherical Fe<sub>3</sub>O<sub>4</sub> NPs, summarized in Table 2. In previous works, the post-synthesis coating with citrate, typically adopted for improving colloidal stability, does not lead to a significant improvement of hyperthermia properties with respect to the uncoated NPs.<sup>71,72</sup> Conversely, the use of chitosan allowed to obtain an increase in SLP around 48%, but this data was found under conditions that exceed the Hergt-Dutz limit.<sup>73</sup> The post-synthesis coating can be also responsible for a detriment of the NP heating efficiency; e.g. a decrease in SLP up to 12%, 26% and 52% was documented for dextran, oleic acid and polyethylene glycol (PEG) treatments, respectively.<sup>71,72,74</sup>

As regards the *in situ* treatment or synthesis process in an environment containing the coating agents, in most cases the NPs synthesized in the presence of citrate, dextran, PEG, polyacrylic acid (PAA) and hyaluronic acid (HA) show lower SLP values than the uncoated NPs.<sup>75,76</sup> In particular, with the *in situ* PAA coating, a 98% lower SLP was obtained, but this is reasonably attributable to the high decrease in the average diameter of the NPs, from 12 nm to 5 nm, and to the final low value of the saturation magnetization.<sup>76</sup> The reduction in SLP can be also correlated to a decrease in the magnetocrystalline anisotropy and thus in the coercivity, as a consequence of the modification of the magnetic order of the surface layers.<sup>75</sup>

Slight improvements in heating efficiency were documented for the *in situ* oleic acid coating of iron oxide NPs with a concentration of 1 % v/v, due to the enhancement in dispersion in water.<sup>77</sup> Very large increases in SLP were observed with the *in situ* coating via polyvinyl pyrrolidone (PVP) or fucoidan treatments, in the order of 60% and 230%, respectively. This was attributed to the role of coating agents in the surface stabilization of NPs, as well as to the growth modifiers acting on the size of NPs, on which the saturation magnetization depends.<sup>76,78</sup>

### 3.5. Analysis of Nanoparticle Solution Stability.

To conclude our experimental studies, we also investigated the stability of the NPs in solution as a crucial parameter for biomedical application development. Figure 6A compares different magnetic suspensions, 6 months after their preparation. In the case of uncoated NPs, we observed their complete precipitation, with sedimentation starting in the first hours after the solution sonication. CMC-coated NPs provided an improved stability, even if sedimentation of a part of them can be observed; the use of sodium-citrate resulted the best solution once again, guaranteeing the NP dispersion as well as their long-term storage without precipitation.

Similar outcomes were observed for the NP encapsulation in hydrogels. After 30 min from the magnetic agarose gel preparation, performed according to the procedure described in Sub-section 2.4, we verified the effective formation of the gels (a comparison of the obtained samples is reported in Figure 6B). Also in this case, the surface coating can play a crucial role in the good dispersion of NPs. While for the uncoated ones, a precipitation of large NP aggregates was observed (possible to be seen by naked eyes at the test tube bottom), sodium-citrate gave the better

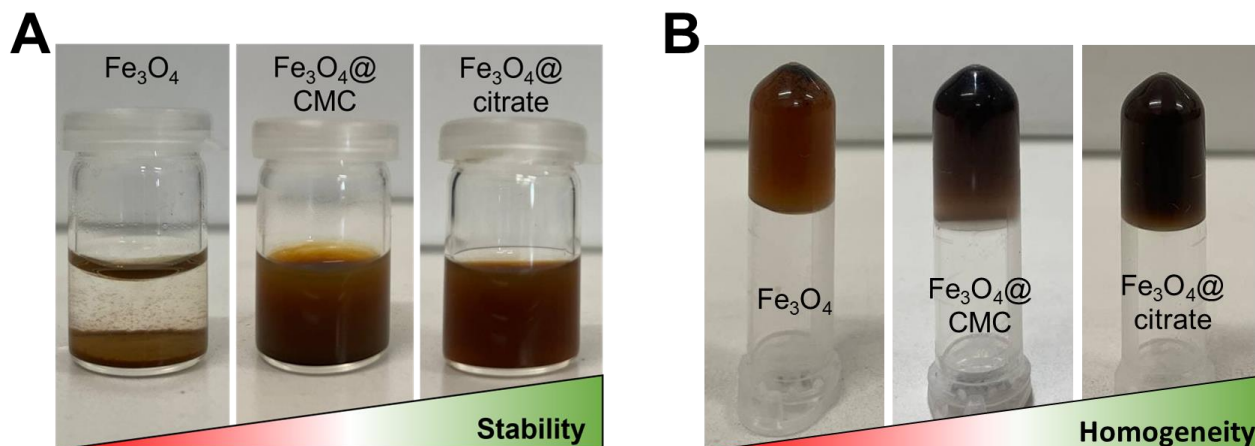


**Figure 6.** (A) Images of magnetic solutions, taken after 6 months from their synthesis. (B) Images of agarose gels with encapsulated NPs. The comparison was made between uncoated, citrate-coated and CMC-coated NPs.

dispersion with a homogeneous distribution of NPs, assessed by optical appearance. This behavior opens to further material development where good dispersion is needed, such as hyperthermia studies in solid environments (to mimic the interaction with biological tissues) or molecule (drugs) release from thermo-responsive gels.

#### 4. CONCLUSIONS

Fe<sub>3</sub>O<sub>4</sub> NPs, with an average size around 10 nm, were synthesized with co-precipitation method and then treated with different surface coatings, based on sodium citrate or CMC. The three obtained samples (uncoated, citrate-coated, and CMC-coated NPs) were investigated for potential application in magnetic hyperthermia, focusing on heating efficiency and colloidal stability.

We demonstrated that both surface coatings can improve the long-term stability and dispersion of the Fe<sub>3</sub>O<sub>4</sub> NPs in solution; moreover, they allow their homogeneous encapsulation in more viscous materials, like hydrogels. The best results were obtained with sodium citrate, which is also able to provide a significant enhancement of the heating efficiency, contrarily to CMC. In particular, the improvement in the dispersion of citrate-coated NPs led to the formation of NP aggregates with smaller dimensions, that in turn generated a strong enlargement of the AC loop area, which consequently led to an increase in SLP in the order of 50% compared to the uncoated NPs.

The results obtained from the complete characterization of the Fe<sub>3</sub>O<sub>4</sub> NPs in terms of structure, size, aggregation state, colloidal stability, as well as magnetic and heating properties, allow to have a broad spectrum of comparison with the literature data, providing additional information for the optimal design of magnetic NPs for hyperthermia applications.

Finally, the obtained results showed how the simple NP synthesis approach here employed, i.e. not requiring any pressure control or high boiling solvents, is a step forward towards reproducibility of preparation procedures in standard chemical laboratories and their possible scalability (demonstrated here at the gram scale) and how a simple coating procedure can significantly increase the SLP values.

## **ASSOCIATED CONTENT**

### **Supporting Information.**

The following files are available free of charge.

TEM images of CMC-coated Fe<sub>3</sub>O<sub>4</sub> NPs (Figure S1); FTIR spectra of uncoated and coated Fe<sub>3</sub>O<sub>4</sub> NPs (Figure S2); Magnetization curve and SLP values of an additional batch of uncoated Fe<sub>3</sub>O<sub>4</sub> NPs (Figure S3); Dynamic hysteresis loops measured on liquid samples containing uncoated and coated Fe<sub>3</sub>O<sub>4</sub> NPs, performed at different values of the AC magnetic field peak amplitude (Figure S4); Time evolutions of the temperature of the magnetic suspensions containing uncoated, citrate-coated and CMC-coated NPs, following the application of an AC magnetic field with different peak amplitudes (Figure S5); SLP values obtained from thermometric measurements at 100 kHz, varying the peak amplitude of the AC magnetic field (Table S1) (PDF).

## **AUTHOR INFORMATION**

### **Corresponding Authors**

Marta Vassallo – Department of Advanced Materials Metrology and Life Science, Istituto Nazionale di Ricerca Metrologica (INRiM), Torino 10135, Italy; Politecnico di Torino, Torino 10129, Italy; ORCID: 0000-0001-9822-9556; Email: [marta.vassallo@polito.it](mailto:marta.vassallo@polito.it)

Alessandra Manzin – Department of Advanced Materials Metrology and Life Science, Istituto Nazionale di Ricerca Metrologica (INRiM), Torino 10135, Italy; ORCID: 0000-0002-4078-2321; Email: [a.manzin@inrim.it](mailto:a.manzin@inrim.it)

### **Authors**

Daniele Martella – Department of Advanced Materials Metrology and Life Science, Istituto Nazionale di Ricerca Metrologica (INRiM), Torino 10135, Italy; European Laboratory for Non-Linear Spectroscopy (LENS), University of Florence, Sesto Fiorentino 50019, Italy;

Gabriele Barrera – Department of Advanced Materials Metrology and Life Science, Istituto Nazionale di Ricerca Metrologica (INRiM), Torino 10135, Italy

Federica Celegato – Department of Advanced Materials Metrology and Life Science, Istituto Nazionale di Ricerca Metrologica (INRiM), Torino 10135, Italy

Marco Coisson – Department of Advanced Materials Metrology and Life Science, Istituto Nazionale di Ricerca Metrologica (INRiM), Torino 10135, Italy

Riccardo Ferrero – Department of Advanced Materials Metrology and Life Science, Istituto Nazionale di Ricerca Metrologica (INRiM), Torino 10135, Italy

Adriano Troia – Department of Advanced Materials Metrology and Life Science, Istituto Nazionale di Ricerca Metrologica (INRiM), Torino 10135, Italy

Hüseyin Sözeri – Magnetism Laboratory, TÜBİTAK Ulusal Metroloji Enstitüsü (UME), Gebze 41470, Kocaeli, Turkey

Camilla Parmeggiani – European Laboratory for Non-Linear Spectroscopy (LENS), University of Florence, Sesto Fiorentino 50019, Italy; Department of Advanced Materials Metrology and Life Science, Istituto Nazionale di Ricerca Metrologica (INRiM), Torino 10135, Italy

Diederik S. Wiersma – European Laboratory for Non-Linear Spectroscopy (LENS), University of Florence, Sesto Fiorentino 50019, Italy; Physics and Astronomy Department, University of Florence, Sesto Fiorentino 50019, Italy; Istituto Nazionale di Ricerca Metrologica (INRiM), Torino 10135, Italy

Paola Tiberto – Department of Advanced Materials Metrology and Life Science, Istituto Nazionale di Ricerca Metrologica (INRiM), Torino 10135, Italy

### **Author Contributions**

The manuscript was written through contributions of all authors. All authors have given approval to the final version of the manuscript.

### **Notes**

The authors declare no competing financial interest.

### **ACKNOWLEDGMENTS**

This work was supported by Project 18HLT06 RaCHy, which has received funding from the European Metrology Programme for Innovation and Research (EMPIR), co-financed by the participating states, and from the European Union's Horizon 2020 Programme.

### **REFERENCES**

- (1) Kozissnik, B.; Bohorquez, A. C.; Dobson, J.; Rinaldi, C. Magnetic fluid hyperthermia: Advances, challenges, and opportunity. *Int. J. Hyperthermia* **2013**, 29(8), 706–714.
- (2) Chang, D.; Lim, M.; Goos, J. A. C. M.; Qiao, R.; Ng, Y.Y.; Mansfeld, F. M.; Jackson, M.; Davis, T. P.; Kavallaris, M. Biologically Targeted Magnetic Hyperthermia: Potential and Limitations. *Front. Pharmacol.* **2018**, 9, 831.
- (3) Bajpai, S.; Tiwary, S. K.; Sonker, M.; Joshi, A.; Gupta, V.; Kumar, Y.; Shreyash, N.; Biswas, S. Recent Advances in Nanoparticle-Based Cancer Treatment: A Review. *ACS Appl. Nano Mater.* **2021**, 4, 6441–6470.
- (4) Khizar, S.; Ahmad, N. M.; Zine, N.; Jaffrezic-Renault, N.; Errachid-el-salhi, A.; Elaissari, A. Magnetic Nanoparticles: From Synthesis to Theranostic Applications. *ACS Appl. Nano Mater.* **2021**, 4, 4284–4306.
- (5) Fernandes Cardoso, V.; Francesko, A.; Ribeiro, C.; Bañobre-López, M.; Martins, P.; Lanceros-Mendez, S. Advances in Magnetic Nanoparticles for Biomedical Applications. *Adv. Healthc. Mater.* **2018**, 7, 1700845.
- (6) Van der Zee, J. Heating the patient: a promising approach? *Ann. Oncol.* **2002**, 13, 1173-1184.
- (7) Dulinska-Litewka, J.; Łazarczyk, A.; Hałubiec, P.; Szafranski, O.; Karnas, K.; Karewicz, A. Superparamagnetic Iron Oxide Nanoparticles-Current and Prospective Medical Applications. *Materials* **2019**, 12 (4), 617.
- (8) Dunn, A. E.; Dunn, D. J.; Lim, M.; Boyerb, C.; Thanh, N. T. K. Recent developments in the design of nanomaterials for photothermal and magnetic hyperthermia induced controllable drug delivery. *Nanoscience* **2013**, 2, 225-254.

- (9) Chiu-Lam, A.; Staples, E.; Pepine, C. J.; Rinaldi, C. Perfusion, cryopreservation, and nanowarming of whole hearts using colloidally stable magnetic cryopreservation agent solutions. *Sci. Adv.* **2021**, *7*, eabe3005.
- (10) Espinosa, A.; Di Corato, R.; Kolosnjaj-Tabi, J.; Flaud, P.; Pellegrino, T.; Wilhelm, C. Duality of Iron Oxide Nanoparticles in Cancer Therapy: Amplification of Heating Efficiency by Magnetic Hyperthermia and Photothermal Bimodal Treatment. *ACS Nano* **2016**, *10* (2), 2436-2446.
- (11) Huang, Y.; Hsu, J. C.; Koo, H.; Cormode, D. P. Repurposing ferumoxytol: Diagnostic and therapeutic applications of an FDA-approved nanoparticle. *Theranostics* **2022**, *12* (2), 796-816.
- (12) Prokopiou, E. D.; Pissas, M.; Fibbi, G.; Margheri, F.; Kalska-Szostko, B.; Papanastasiou, G.; Jansen, M.; Wang, J.; Laurenzana, A.; Efthimiadou, K. E. Synthesis and characterization of modified magnetic nanoparticles as theranostic agents: in vitro safety assessment in healthy cells. *Toxicol. In Vitro* **2021**, *72*, 105094.
- (13) Bobo, D.; Robinson, K. J.; Islam, J.; Thurecht, K. J.; Corrie, S. R. Nanoparticle-Based Medicines: A Review of FDA-Approved Materials and Clinical Trials to Date. *Pharm. Res.* **2016**, *33*, 2373–2387.
- (14) Thiesen, B.; Jordan, A. Clinical applications of magnetic nanoparticles for hyperthermia. *Int. J. Hyperthermia* **2008**, *24* (6), 467-474.
- (15) Johannsen, M.; Thiesen, B.; Wust, P.; Jordan, A. Magnetic nanoparticle hyperthermia for prostate cancer. *Int. J. Hyperthermia* **2010**, *26* (8), 790-795.



- (16) Maier-Hauff, K.; Ulrich, F.; Nestler, D.; Niehoff, H.; Wust, P.; Thiesen, B.; Orawa, H.; Budach, V.; Jordan, A. Efficacy and safety of intratumoral thermotherapy using magnetic iron-oxide nanoparticles combined with external beam radiotherapy on patients with recurrent glioblastoma multiforme. *J. Neurooncol.* **2011**, 103 (2), 317-324.
- (17) Wildeboer, R. R.; Southern, P.; Pankhurst, Q. A. On the reliable measurement of specific absorption rates and intrinsic loss parameters in magnetic hyperthermia materials. *J. Phys. D: Appl. Phys.* **2014**, 47, 495003.
- (18) Tong, S.; Quinto, C. A.; Zhang, L.; Mohindra, P.; Bao, G. Size Dependent Heating of Magnetic Iron Oxide Nanoparticles. *ACS Nano* **2017**, 11, 6808–6816.
- (19) Abenojar, E. C.; Wickramasinghe, S.; Bas-Concepcion, J.; Samia, A. C. S. Structural Effects on the Magnetic Hyperthermia Properties of Iron Oxide Nanoparticles. *Prog. Nat. Sci.: Mater. Int.* **2016**, 26, 440–448.
- (20) Usov, N. A. ; Nesmeyanov, M. S.; Gubanova, E. M.; Epshtein, N. B. Heating ability of magnetic nanoparticles with cubic and combined anisotropy. *Beilstein J. Nanotechnol.* **2019**, 10, 305-314.
- (21) Cabrera, D.; Camarero, J.; Ortega, D.; Teran, F. J. Influence of the aggregation, concentration, and viscosity on the nanomagnetism of iron oxide nanoparticle colloids for magnetic hyperthermia. *J. Nanopart. Res.* **2015**, 17, 121.
- (22) Salas, G.; Camarero, J.; Cabrera, D.; Takacs, H.; Varela, M.; Ludwig, R.; Dähring, H.; Hilger, I.; Miranda, R.; del Puerto Morales, M.; Teran, F. J. Modulation of Magnetic Heating

- via Dipolar Magnetic Interactions in Monodisperse and Crystalline Iron Oxide Nanoparticles. *J. Phys. Chem. C* **2014**, 118, 19985-19994.
- (23) Barrera, G.; Allia, P.; Tiberto, P. Dipolar interactions among magnetite nanoparticles for magnetic hyperthermia: a rate-equation approach. *Nanoscale* **2021**, 13, 4103-4121.
- (24) Darwish, M. S. A.; Kim, H.; Lee, H.; Ryu, C.; Lee, J. Y.; Yoon, J. Synthesis of Magnetic Ferrite Nanoparticles with High Hyperthermia Performance via a Controlled Co-Precipitation Method. *Nanomaterials* **2019**, 9, 1176.
- (25) Balakrishnan, P. B.; Silvestri, N.; Fernandez-Cabada, T.; Marinaro, F.; Fernandes, S.; Fiorito, S.; Miscuglio, M.; Serantes, D.; Ruta, S.; Livesey, K.; Hovorka, O.; Chantrell, R.; Pellegrino, T. Exploiting Unique Alignment of Cobalt Ferrite Nanoparticles, Mild Hyperthermia, and Controlled Intrinsic Cobalt Toxicity for Cancer Therapy. *Adv. Mater.* **2020**, 32, 2003712.
- (26) Ferrero, R.; Barrera, G.; Celegato, F.; Vicentini, M.; Sözeri, H.; Yıldız, N.; Atila Dinçer, C.; Coisson, M.; Manzin, A.; Tiberto, P. Experimental and Modelling Analysis of the Hyperthermia Properties of Iron Oxide Nanocubes. *Nanomaterials* **2021**, 11, 2179.
- (27) Roca, A. G.; Gutiérrez, L.; Gavilán, H.; Fortes Brollo, M. E.; Veintemillas-Verdaguer, S.; Morales, M. D. P. Design strategies for shape-controlled magnetic iron oxide nanoparticles. *Adv. Drug. Deliv. Rev.* **2019**, 138, 68-104.
- (28) Yang, Y.; Liu, X.; Lv, Y.; Heng, T.S.; Xu, X.; Xia, W.; Zhang, T.; Fang, J.; Xiao, W.; Ding, J. Orientation Mediated Enhancement on Magnetic Hyperthermia of Fe<sub>3</sub>O<sub>4</sub> Nanodisc. *Adv. Funct. Mater.* **2015**, 25, 812-820.

- (29) Liu, X.L.; Yang, Y.; Ng, C.T.; Zhao, L.Y., Zhang, Y.; Bay, B.H.; Fan, H.M.; Ding, J. Magnetic Vortex Nanorings: A New Class of Hyperthermia Agent for Highly Efficient In Vivo Regression of Tumors. *Adv. Mater.* **2015**, *27*, 1939–1944.
- (30) Lv, Y.; Yang, Y.; Fang, J.; Zhang, H.; Peng, E.; Liu, X.; Xiao, W.; Ding J. Size dependent magnetic hyperthermia of octahedral Fe<sub>3</sub>O<sub>4</sub> nanoparticles. *RSC Adv.***2015**, *5*, 76764–76771.
- (31) Ferrero, R.; Manzin, A.; Barrera, G.; Celegato, Coïsson, M.; Tiberto, P. Influence of shape, size and magnetostatic interactions on the hyperthermia properties of permalloy nanostructures. *Scientific Reports* **2019**, *9*, 6591.
- (32) Myrovali, E.; Maniotis, N.; Makridis, A.; Terzopoulou, A.; Ntomprougkidis, V.; Simeonidis, K.; Sakellari, D.; Kalogirou, O.; Samaras, T.; Salikhov, R.; Spasova, M.; Farle, M.; Wiedwald, U.; Angelakeris, M. Arrangement at the nanoscale: Effect on magnetic particle hyperthermia. *Scientific Reports* **2016**, *6*, 37934.
- (33) Ruta, S.; Chantrell, R.; Hovorka, O. Unified model of hyperthermia via hysteresis heating in systems of interacting magnetic nanoparticles. *Sci. Rep.* **2015**, *5*, 9090.
- (34) Grüttner, C., Müller, K., Teller, J., Westphal, F. Synthesis and functionalisation of magnetic nanoparticles for hyperthermia applications. *Int. J. Hyperthermia* **2013**, *29* (8), 777-789.
- (35) García-Merino, B., Bringas, E.; Ortiz, I. Synthesis and applications of surface-modified magnetic nanoparticles: progress and future prospects. *Rev. Chem. Eng.* **2021**, 000010151520200072.

- (36) Zhu, N.; Ji, H.; Yu, P.; Niu, J.; Farooq, M. U.; Akram, M. W.; Udego, I. O.; Li, H.; Niu, X. Surface Modification of Magnetic Iron Oxide Nanoparticles. *Nanomaterials* **2018**, 8, 810.
- (37) Garland, E. M.; Parr, J. M.; Williamson, D. S.; Cohen, S. M. In vitro cytotoxicity of the sodium, potassium and calcium salts of saccharin, sodium ascorbate, sodium citrate and sodium chloride. *Toxic. In Vitro* **1989**, 3 (3), 201-205.
- (38) Prokopiou, E. D.; Pissas, M.; Fibbi, G.; Margheri, F.; Kalska-Szostko, B.; Papanastasiou, G.; Jansen, M.; Wang, J.; Laurenzana, A.; Efthimiadou, K. E. Synthesis and characterization of modified magnetic nanoparticles as theranostic agents: in vitro safety assessment in healthy cells. *Toxicol. In Vitro* **2021**, 72, 105094.
- (39) Atrei, A.; Mahdizadeh, F.F.; Baratto, M.C.; Scala, A. Effect of Citrate on the Size and the Magnetic Properties of Primary Fe<sub>3</sub>O<sub>4</sub> Nanoparticles and Their Aggregates. *Appl. Sci.* **2021**, 11, 6974.
- (40) Liu, J.; Sun, Z.; Deng, Y.; Zou, Y.; Li, C.; Guo, X.; Xiong, L.; Gao, Y.; Li, F.; Zhao, D. Highly Water-Dispersible Biocompatible Magnetite Particles with Low Cytotoxicity Stabilized by Citrate Groups. *Angew. Chem. Int. Ed.* **2009**, 48 (32), 5875-5879.
- (41) Blanco-Andujar, C.; Ortega, D.; Southern, P.; Pankhurst, Q. A.; Thanh, N. T. K. High performance multi-core iron oxide nanoparticles for magnetic hyperthermia: microwave synthesis, and the role of core-to-core interactions. *Nanoscale* **2015**, 7 (5), 1768-1775.
- (42) Aguilera, G.; Berry, C. C.; West, R. M.; Gonzalez-Monterrubio, E.; Angulo-Molina, A.; Arias-Carrión, Ó.; Méndez-Rojas, M. Á. Carboxymethyl cellulose coated magnetic

nanoparticles transport across a human lung microvascular endothelial cell model of the blood–brain barrier. *Nanoscale Adv.* **2019**, 1 (2), 671-685.

- (43) Maccarini, M.; Atrei, A.; Innocenti, C.; Barbucci, R. Interactions at the CMC/magnetite interface: Implications for the stability of aqueous dispersions and the magnetic properties of magnetite nanoparticles. *Colloids Surf. A: Physicochem. Eng.* **2014**, 462, 107-114.
- (44) Sitthichai, S.; Pilapong, C.; Thongtem, T.; Thongtem, S. CMC-coated Fe<sub>3</sub>O<sub>4</sub> nanoparticles as new MRI probes for hepatocellular carcinoma. *Appl. Surf. Sci.* **2015**, 356, 972-977.
- (45) Hergt, R.; Dutz, S. Magnetic particle hyperthermia–biophysical limitations of a visionary tumour therapy. *J. Magn. Magn. Mat.* **2007**, 311 (1), 187–192.
- (46) Dutz, S.; Hergt, R. Magnetic nanoparticle heating and heat transfer on a microscale: Basic principles, realities and physical limitations of hyperthermia for tumour therapy. *Int. J. Hyperth.* **2013**, 29 (8), 790–800.
- (47) Rodrigues, H. F.; Capistrano, G.; Bakuzis, A. F. *In vivo* magnetic nanoparticle hyperthermia: a review on preclinical studies, low-field nano-heaters, noninvasive thermometry and computer simulations for treatment planning. *Int. J. Hyperth.* **2020**, 37 (3), 76–99.
- (48) Vicentini, M.; Vassallo, M.; Ferrero, R.; Androulakis, I.; Manzin, A. *In silico* evaluation of adverse eddy current effects in preclinical tests of magnetic hyperthermia. *Comput. Methods Programs Biomed.* **2022**, 223, 106975.

- (49) Manzin, A.; Ferrero, R.; Vicentini, M. From Micromagnetic to *In Silico* Modeling of Magnetic Nanodisks for Hyperthermia Applications. *Advanced Theory and Simulations* **2021**, 4 (5), 2100013.
- (50) Tay, Z. W.; Chandrasekharan, P.; Chiu-Lam, A.; Hensley, D. W.; Dhavalikar, R.; Zhou, X. Y.; Yu, E. Y.; Goodwill, P. W.; Zheng, B.; Rinaldi, C.; Conolly, S. M. Magnetic Particle Imaging-Guided Heating in Vivo Using Gradient Fields for Arbitrary Localization of Magnetic Hyperthermia Therapy. *ACS Nano* **2018**, 12 (4), 3699-3713.
- (51) Schneider, C.A.; Rasband, W.S.; Eliceiri, K.W. NIH Image to ImageJ: 25 years of image analysis. *Nat. Methods* **2012**, 9, 671–675.
- (52) Coïsson, M.; Barrera, G.; Celegato, F.; Martino, L.; Kane, S. N.; Raghuvanshi, S.; Vinai, F.; Tiberto, P. Hysteresis losses and specific absorption rate measurements in magnetic nanoparticles for hyperthermia applications. *Biochim. Biophys. Acta* **2017**, 1861 (6), 1545-1558.
- (53) Coïsson, M.; Barrera, G.; Appino, C.; Celegato, F.; Martino, L.; P. Safronov, A. P.; Kurlyandskaya, G. V.; Tiberto, P. Specific loss power measurements by calorimetric and thermal methods on  $\gamma$ -Fe<sub>2</sub>O<sub>3</sub> nanoparticles for magnetic hyperthermia. *J. Magn. Magn. Mater.* **2019**, 473, 403-409.
- (54) Nigam, S.; Barick, K. C.; Bahadur, D. Development of citrate-stabilized Fe<sub>3</sub>O<sub>4</sub> nanoparticles: Conjugation and release of doxorubicin for therapeutic applications. *J. Magn. Magn. Mater.* **2011**, 323 (2), 237-243.

- (55) Srivastava, S.; Awasthi, R.; Gajbhiye, N. S.; Agarwal, V.; Singh, A.; Yadav, A.; Gupta, R. K. Innovative synthesis of citrate-coated superparamagnetic Fe<sub>3</sub>O<sub>4</sub> nanoparticles and its preliminary applications. *J. Colloid. Interf. Sci.* **2011**, 359 (1), 104-111.
- (56) Cai, Y.; Yuan, F.; Wang, X.; Sun, Z.; Chen, Y.; Liu, Z.; Wang, X.; Yang, S.; Wang, S. Synthesis of core-shell structured Fe<sub>3</sub>O<sub>4</sub>@carboxymethyl cellulose magnetic composite for highly efficient removal of Eu(III). *Cellulose* **2017**, 24, 175–190.
- (57) Cortés-Llanos, B.; Ocampo, S. M.; De la Cueva, L.; Calvo, G. F.; Belmonte-Beitia, J.; Pérez, L.; Salas, G.; Ayuso-Sacido, A. Influence of Coating and Size of Magnetic Nanoparticles on Cellular Uptake for In Vitro MRI. *Nanomaterials* **2021**, 11, 2888.
- (58) Marsalek, R. Particle size and Zeta Potential of ZnO. *APCBEE Procedia* **2014**, 9, 13-17.
- (59) Feng, J.; Mao, J.; Wen, X.; Tu, M. Ultrasonic-assisted in situ synthesis and characterization of superparamagnetic Fe<sub>3</sub>O<sub>4</sub> nanoparticles. *J. Alloys Compd.* **2011**, 509 (37), 9093-9097.
- (60) Zhang, H.; Zeng, D.; Liu, Z. The law of approach to saturation in ferromagnets originating from the magnetocrystalline anisotropy. *J. Magn. Magn. Mater.* **2010**, 322, 2375–2380.
- (61) Cullity, B. D.; Graham, C. D. *Introduction to Magnetic Materials*; Wiley, **2009**.
- (62) Sciancalepore, C.; Gualtieri, A. F.; Scardi, P.; Flor, A.; Allia, P.; Tiberto, P.; Barrera, G.; Messori, M.; Bondioli, F. Structural characterization and functional correlation of Fe<sub>3</sub>O<sub>4</sub> nanocrystals obtained using 2-ethyl-1,3-hexanediol as innovative reactive solvent in non-hydrolytic sol-gel synthesis. *Mater. Chem. Phys.* **2018**, 207, 337-349.

- (63) Chen, J. P.; Sorensen, C. M.; Klabunde, K. J.; Hadjipanayis, G. C.; Devlin, E.; Kostikas, A. Size-dependent magnetic properties of  $\text{MnFe}_2\text{O}_4$  fine particles synthesized by coprecipitation. *Phys. Rev. B* **1996**, 54 (13), 9288-9296.
- (64) Lima, E. Jr.; Brandl, A. L.; Arelaro, A. D.; Goya, G. F. Spin disorder and magnetic anisotropy in  $\text{Fe}_3\text{O}_4$  nanoparticles. *J. Appl. Phys.* **2006**, 99, 083908.
- (65) Nemala, H.; Thakur, J. S.; Naik, V. M.; Vaishnava, P. P.; Lawes, G.; Naik, R. Investigation of magnetic properties of  $\text{Fe}_3\text{O}_4$  nanoparticles using temperature dependent magnetic hyperthermia in ferrofluids. *J. Appl. Phys.* **2014**, 116, 034309.
- (66) Nayek, C.; Manna, K.; Imam, A. A.; Alqasrawi, A. Y.; Obaidat, I. M. Size-dependent magnetic anisotropy of PEG coated  $\text{Fe}_3\text{O}_4$  nanoparticles; comparing two magnetization methods. *IOP Conf. Ser.: Mater. Sci. Eng.* **2018**, 305, 012012.
- (67) Allia, P.; Coisson, M.; Knobel, M.; Tiberto, P.; Vinai, F. Magnetic hysteresis based on dipolar interactions in granular magnetic systems. *Phys. Rev. B* **1999**, 60 (17), 12207-12218.
- (68) Barrera, G.; Coisson, M.; Celegato, F.; Martino, L.; Tiwari, P.; Verma, R.; Kane, S. N.; Mazaleyrat, F.; Tiberto, P. Specific Loss Power of Co/Li/Zn-Mixed Ferrite Powders for Magnetic Hyperthermia. *Sensors* **2020**, 20, 2151.
- (69) Ota, S.; Takemura, Y. Dynamics of magnetization and easy axis of individual ferromagnetic nanoparticle subject to anisotropy and thermal fluctuations. *J. Magn. Soc. Jpn.* **2019**, 43, 34-41.
- (70) Barrera, G.; Allia, P.; Tiberto, P. Heating ability modulation by clustering of magnetic particles for precision therapy and diagnosis. *J. Phys. D: Appl. Phys.* **2021**, 54, 315003.



- (71) Ognjanović, M.; Stanković, D. M.; Jaćimović, Z. K.; Kosović-Perutović, M.; Dojčinović, B.; Antić, B. The effect of surface-modifier of magnetite nanoparticles on electrochemical detection of dopamine and heating efficiency in magnetic hyperthermia. *J. Alloys Compd.* **2021**, 884, 161075.
- (72) Soares, P. I. P.; Lochte, F.; Echeverria, C.; Pereira, L. C. J.; Coutinho, J. T.; Ferreira, I. M. M.; Novo, C. M. M.; Borges, J. P. M. R. Thermal and magnetic properties of iron oxide colloids: influence of surfactant. *Nanotechnology* **2015**, 26, 425704.
- (73) Shete, P. B.; Patil, R. M.; Thorat, N. D.; Prasad, A.; Ningthoujam, R. S.; Ghosh, S. J.; Pawar, S. H. Magnetic chitosan nanocomposite for hyperthermia therapy application: Preparation, characterization and in vitro experiments. *App. Surf. Sci.* **2014**, 288, 149-157.
- (74) Ghosh, R.; Pradhan, L.; Devi, Y. P.; Meena, S. S.; Tewari, R.; Kumar, A.; Sharma, S.; Gajbhiye, N. S.; Vatsa, R. K.; Pandey, B. N.; Ningthoujam, R. S. Induction heating studies of Fe<sub>3</sub>O<sub>4</sub> magnetic nanoparticles capped with oleic acid and polyethylene glycol for hyperthermia. *J. Mater. Chem.* **2011**, 21, 13388.
- (75) Simeonidis, K.; Liébana-Vinas, S.; Wiedwald, U.; Ma, Z.; Li, Z.-A.; Spasova, M.; Patsia, O.; Myrovali, E.; Makridis, A.; Sakellari, D.; Tsiaoussis, I.; Vourlias, G.; Farle, M.; Angelakeris, M. A versatile large-scale and green process for synthesizing magnetic nanoparticles with tunable magnetic hyperthermia features. *RCS Adv.* **2016**, 6, 53107-53117.
- (76) El-Boubbou, K.; Lemine, O. M.; Ali, R.; Huwaizi, S. M.; Al-Humaid S.; AlKushi, A. Evaluating magnetic and thermal effects of various Polymerylated magnetic iron oxide nanoparticles for combined chemo-hyperthermia. *New J. Chem.* **2022**, 46, 5489.

- (77) Şentürk, F.; Çakmak, S.; Ozturk, G. G. Synthesis and Characterization of Oleic Acid Coated Magnetic Nanoparticles for Hyperthermia Applications. *J. Nat. Appl. Sci.* **2019**, 2(2), 16-29.
- (78) Gonçalves, J.; Nunes, C.; Ferreira, L.; Cruz, M. M.; Oliveira, H.; Bastos, V.; Mayoral, A.; Zhang, Q.; Ferreira, P. Coating of Magnetite Nanoparticles with Fucoidan to Enhance Magnetic Hyperthermia Efficiency. *Nanomaterials* **2021**, 11, 2939.